were summed as: $\sum^{k\in O_2,\text{even}} x^k_{j,(2,t)}$ and $\sum^{k\in H_2O,\text{even}} x^k_{j,(2,t)}$. Lastly, all the odd-numbered frames were summed as: $\sum^{k\in O_2,\text{odd}} x^k_{j,(1,t)}$ and $\sum^{k\in H_2O,\text{odd}} x^k_{j,(1,t)}$. We assumed two images summed with even- and odd-numbered frames are physiologically and quantitatively equivalent and statistically independent.

Arterial blood TACs were corrected for radioactivity decay and dispersion ($\tau = 4$ s) [4, 13, 14] and delay [3, 4, 15] further, the $^{15}O_2$ and $H_2^{15}O$ contents were separated [11]. The obtained $^{15}O_2$ and $H_2^{15}O$ arterial TACs were used as the water and oxygen input functions as $A_W(t)$ and $A_O(t)$, respectively.

Sets of CBF, OEF and $CMRO_2$ images were generated using the DARG approach as described previously [4] by using a set of summed images in both the oxygen and water phases ($\sum^{k\in O_2,\rho} x^k_{j,(1,t)}$ and $\sum^{k\in H_2O,\rho} x^k_{j,(1,t)}$, where ρ indicates the rule of sum, i.e., all, even or odd), $^{15}O_2$ and $H_2^{15}O$ input functions [$A_W(t)$ and $A_O(t)$] and cerebral blood volume (CBV) image that was obtained from the $C^{15}O$ scan data [3, 4]. This procedure was repeated for all sets of images and the functional images for jth pixel were obtained as: $CBF^{\rho}_{j,(i,t)}$, $OEF^{\rho}_{j,(i,t)}$ and $CMRO^{\rho}_{2j,(i,t)}$, where indices (i, t) are same as those for AC, and ρ is the rule of sum.

Dependency of quantitative CBF/OEF/$CMRO_2$ accuracy on the transmission true counts

An ROI was placed on the frontal, temporal and parietal cortical region (5000–10000 pixels) of the image and the CBF, OEF and $CMRO_2$ values were extracted from all the datasets. The mean of these extracted values was expressed as the percent difference between the values obtained from the functional images computed with $AC_1^t$and with AC_1^{600s} for all datasets obtained from the emission data as:

$$\frac{R\left[\text{Func}^{\text{all}}{}_{j,(1,t)}\right] - R\left[\text{Func}^{\text{all}}_{j,(1,600s)}\right]}{R\left[\text{Func}^{\text{all}}_{j,(1,600s)}\right]} \times 100\% \quad (4)$$

where R indicates mean pixel value inside the ROI and Func indicates either CBF, OEF or $CMRO_2$.

Dependency of CBF/OEF/$CMRO_2$ image quality on the transmission true counts

Subtracted images were created by subtracting the functional images between even- and odd-numbered frames as;

$$I^{\text{Func}}_{j,t} = \text{Func}^{\text{even}}_{j,(1,t)} - \text{Func}^{\text{odd}}_{j,(2,t)} \quad (5)$$

for the jth pixel. The N-index in the ROI, placed on the frontal, temporal and parietal cortical region as above, for these subtracted images were calculated as:

$$\text{NI}^t_{\text{Func}} = \text{SD}_{j\in\text{ROI}}\left[I^{\text{Func}}_{j,t}\right]. \quad (6)$$

The obtained N-indices were expressed as a function of the total true count of the transmission scan data.

Results

Phantom studies for validation of N-index

Figure 1 shows representative slices of the obtained images of mean, SD, and subtraction. The later scan has more noise due to count statistics, which can be observed in SD image and the subtracted images in Fig. 1. Despite the difference in the activity distribution, the SD image was almost uniform. The relationship between the mean value of the SD image (M_{SD}) and N-index (NI) in the same ROI

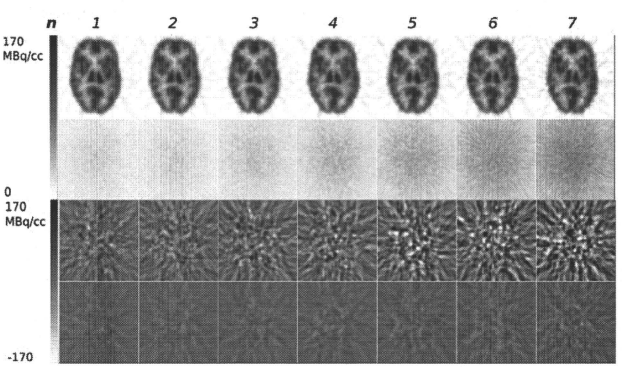

Fig. 1 Representative slices of the reconstructed images obtained from the phantom studies. The *first row* is averaged image, the *second row* is SD image, the *third row* is the subtracted image for the dataset (a), and the *fourth row* is the subtracted image for the dataset (b). *Each column* corresponds the images from nth scan (total seven scans)

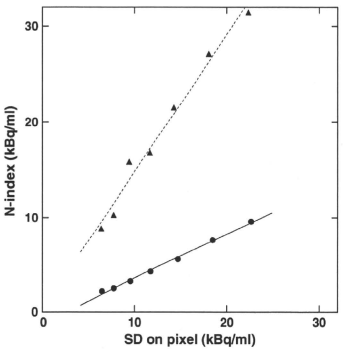

Fig. 2 The relationship between the mean SD value and *N*-index obtained from the subtracted image with the same ROI region of the brain phantom. The regression line was expressed as $y = 1.44x - 0.331$ (kBq/ml) ($r = 0.99$, $n = 7$). and $y = 0.47x - 1.29$ (kBq/ml) ($r = 0.99$, $n = 7$), for 5 s (*closed triangle*) and 125 s (*closed circle*) in calculating *N*-index, respectively

is shown in Fig. 2. The regression line is expressed as $NI = 1.44M_{SD} - 0.331$ (kBq/ml) ($r = 0.99$) and $NI = 0.47M_{SD} - 1.285$ (kBq/ml) ($r = 0.99$), where r is correlation coefficient, for the subtracted images obtained from the 5- and 125-s data, respectively. The results shown in Figs. 1 and 2 support the assumption that the SD of the pixel value is uniform in a non-homogeneous image that was reconstructed using the FBP method. Furthermore, the present *N*-index was correlated with the SD and could be employed to compare the image qualities.

Dependency of quantitative CBF/OEF/$CMRO_2$ accuracy on the transmission true counts

Figure 3 shows the percent difference in the CBF (a), OEF (b) and $CMRO_2$ (c) values when compared with those computed using the 10-min AC map. The results show that the quantitative values obtained during the CBF, OEF and $CMRO_2$ measurements are almost identical, namely, difference was <5% to those obtained when AC was performed using the transmission data containing true counts more than 40 Mcounts.

Dependency of the CBF/OEF/$CMRO_2$ image quality on the transmission true counts

Figure 4 shows the *N*-indices in the CBF (a), OEF (b) and $CMRO_2$ (c) images, as a function of the number of true counts of the transmission data. The present results show that the qualities of the CBF, OEF and $CMRO_2$ images

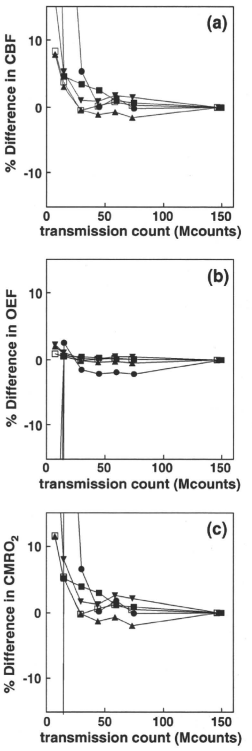

Fig. 3 Percent difference in the CBF, OEF and $CMRO_2$ values when compared with those obtained from the 10-min transmission data, as a function of the true counts of the transmission data. Each type of *symbol* corresponds to each subject ($n = 6$). The indicated values were extracted from the ROI in the frontal, parietal and temporal cortex regions

were almost equal to those in which the true counts of the transmission data used exceeded 40 Mcounts.

Discussion and conclusion

Our purpose of this study was to shorten the transmission scan duration for ^{15}OPET study with DARG measurement. By evaluating bias and noise on the functional images of the CBF, OEF and $CMRO_2$ due to noise in transmission data, optimal transmission true count in DARG measurement was

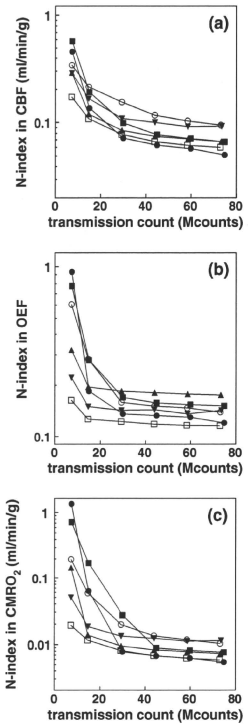

Fig. 4 The *N*-indices for the CBF, OEF and $CMRO_2$ images that were obtained from various true counts of the transmission data as a function of the true counts of the transmission data. Each type of *symbol* corresponds to each subject ($n = 6$). The *symbols* used and ROI are the same as that used for Fig. 3

determined. We found 40 Mcounts of the true count in the transmission scan was optimal, and consequently, we were able to shorten the total duration of the DARG examination.

We introduced the *N*-index to compare the noise level on inhomogeneous functional images. The benefit of using *N*-index is that by one index number, one can characterize the noise in functional image derived from PET data and DARG measurement which have complex noise propagations from several error sources. The validity of the *N*-index was tested in the phantom study. We found tight correlation between pixel noise and the *N*-index.

The present result using the brain phantom supported the assumption that the SD of a pixel value was spatially uniform even in a non-homogeneous region of an FBP reconstructed image (Fig. 1). Furthermore, the regression line between the SD value from the statistically obtained SD image and the *N*-index from the subtracted image for 5- and 125-s data were highly correlated ($r = 0.99$) (Fig. 2). The slope for 5-s data was approximately $\sqrt{2}$, where the SD of the image obtained by subtraction of two 5-s data (statistically corresponding to 10 s) could be expected to be $\sqrt{2}$ greater than that of the original image. For 125-s data, 1/5 of statistical noise compared to 5-s data is expected. However, *N*-index for 125-s data overestimated in 18% in average than expected. One possible reason of this overestimation is influence of inhomogeneity of the reconstructed image. Therefore, the *N*-index cannot be used to estimate absolute noise level in the image, but the *N*-index is still valid for study which compares relative noise levels among multiple images.

Using the *N*-index, we examined the change of image quality in the CBF, OEF and $CMRO_2$ as the noise level based on the change in the true counts of the transmission data. One of the advantages using the *N*-index is that it allows us to compare the noise level of non-uniform images such as that of the brain, using the data obtained by ordinal PET scan procedure. In order to investigate the noise level of the PET images using parameters other than the *N*-index, the PET scans must be replicated for a human subject. However, this appears unlikely due to the excessive radiation dose that would need to be administered to the subject. Furthermore, it might be quite hard to maintain the equivalent measurement conditions such as the radiation dose, as well as the physiological conditions of the subjects.

In this study, two implicit conditions were assumed: the SD on pixel value is uniform for the targeted region and odd-and even-numbered frames have the same statistical properties. The condition of uniform distribution of the SD on the functional image might not be microscopically fulfilled due to nature of nonlinearity of DARG method. However, in global, noise on the reconstructed image could be linearly propagated to the functional image and we considered this assumption was valid for computing the *N*-index. The *N*-index can be applied to other cases such as a variety of tracers and organs in order to examine the image quality as far as those conditions are satisfied. It should be noted that the CBF and $CMRO_2$ parametric images are required to be assessed quantitatively [16], thus the present study was validated with images reconstructed by FBP method. Limitation of the present method is that the *N*-index may not be applied to images such as those reconstructed by the maximum likelihood expectation maximization based algorithm, because the uniformity of SD across pixels is not guaranteed. However, a similar procedure of the present method still has possibility to be

applied, if, for example, coefficient of variation is uniform across pixels.

When *N*-index was estimated from two images with either emission or transmission data being common, the variation on image can be calculated as a sum of each variation and subtraction of covariance, canceling effect of noise from common data. Consequently, the *N*-index only reflects noise on either transmission or emission data. Thus, we estimated *N*-index by subtracting fully independent images. The validity of *N*-index could be tested in the phantom study using common transmission data; however, we still computed *N*-index using fully independent images, because the test should be done in the same conditions as the experimental study.

The present results showed that poor count statistics in transmission scanning resulted in significant bias in quantitative values of CBF, OEF and $CMRO_2$. As has been mathematically described [17], AC factor, i.e. blank/transmission is biased by factor of $(1 + 1/m)$, where m is a transmission count on a corresponding pixel. Therefore, the poorer the transmission scan count is, the higher the AC factor becomes. In view of image quality, noise in transmission data influences functional image as shown in Fig. 4. On the other hand, as indicated in Fig. 4, extra longer transmission scan gains no statistical benefit. The optimized transmission scan duration will be determined by relative noise level of the transmission data against the emission data.

In this paper, we used fixed duration of 600 s of the transmission scan for CO image, assuming little effect of noise on CO image. One reason for this assumption is that 50% error in CBV value derives around only 3% error in OEF and $CMRO_2$ images [4], suggesting 50% noise on CBV image resulting only 3% noise on OEF and $CMRO_2$ images. As shown in Fig. 4, the degree of noise on the OEF and $CMRO_2$ images are around 20–25%, and the level of noise is quite high compared to level of noise from CBV image.

Motion of subject, during a scan, could be a problem to calculate *N*-index. However, movement of a subject during a scan affects both the odd-and even-numbered frames simultaneously, and thus the statistical properties between two summed images will stay the same. Thus, motion of a subject during a scan might not be that critical with regards to the *N*-index, as far as the motion does not deteriorate the image used to assess the function of the targeted organ.

The comparison of the *N*-indices between subjects or between different functional images cannot be performed because the *N*-indices offer information of relative noise level but not absolute noise. Thus, a meaningful comparison can be made between images of the same subject and of the same cerebral function (such as CBF and $CMRO_2$).

It is generally accepted that accurate ACs require transmission scanning using external sources [6, 7], although there are excellent techniques designed to shorten or eliminate the transmission scan duration, such as the transmission-data-based segmented method for the AC map [18, 19] or the emission-based AC map calculation [20]. The present approach might be applicable to investigate the noise level in segmented or emission-based methods, which should enable us to further shorten the duration of a PET examination.

Boellaard et al. demonstrated the relationship between the transmission scan counts and phantom diameter, and they found that this relationship did not restrict the application of the count-based transmission scans for correcting the reduction in the rod source strength [21]. However, they indicated that when the subject is extremely small, a transmission scan based on an acquired number of true counts should not be applied. This is because the counts for lines of response not passing through the subject would increase. Further studies are required to determine the optimal examination conditions for such situations.

We found that the true counts of the transmission data exceeding 40 millions (corresponds to 3 min scan in this study) were appropriate for the CBF, OEF and $CMRO_2$ measurement by DARG method in terms of both quantitative accuracy and image quality, consequently we can shorten the examination duration for obtaining those images. Conventional DARG measurement in clinical study uses 10 min of transmission scan, while 9 min of emission scan of dual tracers of $^{15}O_2$ and $H_2^{15}O$, in addition to 4 min of $C^{15}O$ scan [22]. If one can shorten the transmission scan to 3 min, total scan duration is 16 min (30% reduction). Currently, another $C^{15}O$ scan for CBV correction with regards to the assessment of CBF, OEF and $CMRO_2$ is still required, an additional mathematical formulation strategy, like the basis function method [23] could eliminate this requirement [5].

In conclusion, we determined the required transmission true count that maintains the quantitative accuracy and image quality for PET studies with $H_2^{15}O$ and $^{15}O_2$. According to our results, the total study duration could be minimized by shortening the transmission scan. Although the obtained results in the present study were measurement condition specific, the *N*-index could be used to determine PET scanning procedures.

Acknowledgments The authors would like to thank Ms Atra Ardakani for her invaluable help on preparing this article. The authors gratefully acknowledge the staff of the Department of Nuclear Medicine, Hospital and the Department of Investigative Radiology, Research Institute, National Cardiovascular Center. The present work was supported by the Program for Promotion of Fundamental Studies in Health Science of the Organization for Pharmaceuticals and

Medical Devices Agency of Japan (PMDA), and the Nakatani Electronic Measuring Technology Association of Japan, and by the Ministry of Education, Science, Sports and Culture, Grant-in-Aid for Young Scientists (start-up), 21890171, 2009.

References

1. Mintun M, Raichle M, Martin W, Herscovitch P. Brain oxygen utilization measured with O-15 radiotracers and positron emission tomography. J Nucl Med. 1984;25:177–87.
2. Hatazawa J, Fujita H, Kanno I, Satoh T, Iida H, Miura S, et al. Regional cerebral blood flow, blood volume, oxygen extraction fraction, and oxygen utilization rate in normal volunteers measured by the autoradiographic technique and the single breath inhalation method. Ann Nucl Med. 1995;9:15–21.
3. Shidahara M, Watabe H, Kim K, Oka H, Sago M, Hayashi T, et al. Evaluation of a commercial PET tomograph-based system for the quantitative assessment of rCBF, rOEF and rCMRO2 by using sequential administration of 15O-labeled compounds. Ann Nucl Med. 2002;16:317–27.
4. Kudomi N, Hayashi T, Teramoto N, Watabe H, Kawachi N, Ohta Y, et al. Rapid quantitative measurement of CMRO(2) and CBF by dual administration of (15)O-labeled oxygen and water during a single PET scan—a validation study and error analysis in anesthetized monkeys. J Cereb Blood Flow Metab. 2005;25:1209–24.
5. Kudomi N, Hayashi T, Watabe H, Iida H. Rapid CBF/$CMRO_2$ measurement in a single PET scan with dual tracer administration. J Cereb Blood Flow Metab. 2005;25:S672.
6. Bailey D. Transmission scanning in emission tomography. Eur J Nucl Med. 1998;25:774–87.
7. Ostertag H, Kbler W, Doll J, Lorenz W. Measured attenuation correction methods. Eur J Nucl Med. 1989;15:722–6.
8. Watabe H, Matsumoto K, Senda M, Iida HP. Performance of list mode data acquisition with ECAT EXACT HR and ECAT EXACT HR + positron emission scanners. Ann Nucl Med. 2006;20:189–94.
9. Hoffman E, Cutler P, Digby W, Mazziotta J. 3-D phantom to simulate cerebral blood flow and metabolic images for PET. IEEE Trans Nucl Sci. 1990;37:616–20.
10. Pajevic S, Daube-Witherspoon M, Bacharach S, Carson R. Noise characteristics of 3-D and 2-D PET images. IEEE Trans Med Imaging. 1998;17:9–23.
11. Kudomi N, Watabe H, Hayashi T, Iida H. Separation of input function for rapid measurement of quantitative $CMRO_2$ and CBF in a single PET scan with a dual tracer administration method. Phys Med Biol. 2007;52:1893–908.
12. Kudomi N, Choi E, Yamamoto S, Watabe H, Kim K, Shidahara M, et al. Development of a GSO detector assembly for a continuous blood sampling system. IEEE Trans Nucl Sci. 2003;50:70–3.
13. Iida H, Kanno I, Miura S, Murakami M, Takahashi K, Uemura K. Error analysis of a quantitative cerebral blood flow measurement using H2(15)O autoradiography and positron emission tomography, with respect to the dispersion of the input function. J Cereb Blood Flow Metab. 1986;6:536–45.
14. Lammertsma A, Cunningham V, Deiber M, Heather J, Bloomfield P, Nutt J, et al. Combination of dynamic and integral methods for generating reproducible functional CBF images. J Cereb Blood Flow Metab. 1990;10:675–86.
15. Iida H, Higano S, Tomura N, Shishido F, Kanno I, Miura S, et al. Evaluation of regional differences of tracer appearance time in cerebral tissues using [15O] water and dynamic positron emission tomography. J Cereb Blood Flow Metab. 1988;8:285–8.
16. Ibaraki M, Miura S, Shimosegawa E, Sugawara S, Mizuta T, Ishikawa A, et al. Quantification of cerebral blood flow and oxygen metabolism with 3-dimensional PET and 15O: validation by comparison with 2-dimensional PET. J Nucl Med. 2007;49:50–9.
17. Freedman N, Bacharach S, Carson R, Price J, Dilsizian V. Effect of smoothing during transmission processing on quantitative cardiac PET scans. J Nucl Med. 1996;37:690–4.
18. Xu M, Luk W, Cutler P, Digby W. Local threshold for segmented attenuation correction of PET imaging of the thorax. IEEE Trans Nucl Sci. 1994;41:1532–7.
19. Xu M, Cutler P, Luk W. Adaptive, segmented attenuation correction for whole-body PET imaging. IEEE Trans Nucl Sci. 1996;43:331–6.
20. Weinzapfel B, Hutchins G. Automated PET attenuation correction model for functional brain imaging. J Nucl Med. 2001;42:483–91.
21. Boellaard R, Lingen Av, Balen Sv, Lammertsma A. Optimization of attenuation correction for positron emission tomography studies of thorax and pelvis using count-based transmission scans. Phys Med Biol. 2004;49:N31–8.
22. Iwanishi K, Watabe H, Hayashi T, Miyake Y, Minato K, Iida H. Influence of residual oxygen-15-labeled carbon monoxide radioactivity on cerebral blood flow and oxygen extraction fraction in a dual-tracer autoradiographic method. Ann Nucl Med. 2009;23:363–71.
23. Gunn R, Lammertsma A, Hume S, Cunningham V. Parametric imaging of ligand receptor binding in PET using a simplified reference region model. Neuroimage. 1997;6:279–87.

Multicenter Evaluation of a Standardized Protocol for Rest and Acetazolamide Cerebral Blood Flow Assessment Using a Quantitative SPECT Reconstruction Program and Split-Dose ^{123}I-Iodoamphetamine

Hidehiro Iida[1,2], Jyoji Nakagawara[1,3], Kohei Hayashida[1,4], Kazuhito Fukushima[1,5], Hiroshi Watabe[1,2], Kazuhiro Koshino[1,2], Tsutomu Zeniya[1,2], and Stefan Eberl[1,6]

[1]Dual-Table Autoradiography SPECT Research Group in Japan, Osaka, Japan; [2]National Cerebral and Cardiovascular Center–Research Institute, Osaka, Japan; [3]Nakamura Memorial Hospital, Sapporo, Japan; [4]Takeda Hospital, Kyoto, Japan; [5]National Cerebral and Cardiovascular Center–Hospital, Osaka, Japan; and [6]Royal Prince Alfred Hospital, Sydney, Australia

SPECT can provide valuable diagnostic and treatment response information in large-scale multicenter clinical trials. However, SPECT has been limited in providing consistent quantitative functional parametric values across the centers, largely because of a lack of standardized procedures to correct for attenuation and scatter. Recently, a novel software package has been developed to reconstruct quantitative SPECT images and assess cerebral blood flow (CBF) at rest and after acetazolamide challenge from a single SPECT session. This study was aimed at validating this technique at different institutions with a variety of SPECT devices and imaging protocols. **Methods:** Twelve participating institutions obtained a series of SPECT scans on physical phantoms and clinical patients. The phantom experiments included the assessment of septal penetration for each collimator used and of the accuracy of the reconstructed images. Clinical studies were divided into 3 protocols, including intrainstitutional reproducibility, a comparison with PET, and rest–rest study consistency. The results from 46 successful studies were analyzed. **Results:** Activity concentration estimation (Bq/mL) in the reconstructed SPECT images of a uniform cylindric phantom showed an interinstitution variation of ±5.1%, with a systematic underestimation of concentration by 12.5%. CBF values were reproducible both at rest and after acetazolamide on the basis of repeated studies in the same patient (mean ± SD difference, −0.4 ± 5.2 mL/min/100 g, n = 44). CBF values were also consistent with those determined using PET (−6.1 ± 5.1 mL/min/100 g, n = 6). **Conclusion:** This study demonstrates that SPECT can quantitatively provide physiologic functional images of rest and acetazolamide challenge CBF, using a quantitative reconstruction software package.

Key Words: ^{123}I-iodoamphetamine; cerebral blood flow; acetazolamide; SPECT; vascular reactivity; quantitation

J Nucl Med 2010; 51:1624–1631
DOI: 10.2967/jnumed.110.078352

Received Apr. 27, 2010; revision accepted Jul. 14, 2010.
For correspondence or reprints contact: Hidehiro Iida, Department of Investigative Radiology, National Cerebral and Cardiovascular Center–Research Institute, 5-7-1 Suita City, Osaka 565-8565, Japan.
E-mail: iida@ri.ncvc.go.jp

Current clinical practice using SPECT relies largely on interpretation of qualitative images reflecting physiologic function. Quantitative functional parametric images may be obtained by applying mathematic modeling to SPECT data corrected for attenuation and scatter. Quantitative regional cerebral blood flow (CBF) (*1–3*) and cerebral vascular reactivity (CVR) in response to acetazolamide challenge (*4–6*) have been obtained with these techniques. One major application of such quantitative SPECT (QSPECT) approaches is the evaluation of ischemic status in patients with occlusion or stenosis in their middle cerebral arteries, to provide prognostic information of the outcome of revascularization therapies (*7*). Quantitative analysis in SPECT has also been demonstrated in the assessment of binding potential for several neuroreceptor ligands (*8,9*), for the quantitative assessment of regional myocardial perfusion (*10,11*), and for the assessment of radioaerosol deposition and clearance in healthy and diseased lungs (*12*). However, providing the standardized quantitative approach required for multicenter clinical trials has so far received only limited attention. Challenges remain in providing consistent quantitative data across institutions using a variety of SPECT equipment and vendor-specific reconstruction strategies (*13*). This limitation is attributed to a lack of standardized procedures in the reconstruction software offered by vendors, particularly in terms of correcting attenuation and scatter. Kinetic modeling for physiologic parameter estimation is also not part of the vendors' standard SPECT software. Although separate packages can be purchased for this purpose, they are not integrated and are flexible general-purpose packages, requiring considerable skill and knowledge to effectively use. Thus, they are not ideal for routine clinical use.

Scatter and attenuation occur in the object and are thus object-dependent but are not dependent on the geometry of the imaging equipment (*14*). Therefore, once a software program is developed to provide accurate image reconstruction with compensation for both attenuation and scatter, the

program should be able to provide quantitative images that are intrinsically independent of the geometric design of SPECT cameras. This is an attractive feature of SPECT for multicenter clinical studies.

From the various techniques available to correct for attenuation (*15*) and scatter (*16*), one feasible approach for clinical studies is based on a combination of attenuation correction, incorporated into the ordered-subset expectation maximization (OSEM) reconstruction (*17*), and scatter correction by the transmission-dependent convolution subtraction (TDCS) originally proposed by Meikle et al. (*18*). This approach has been extensively investigated by our group (*11,19*) for ^{99m}Tc for studies of the brain and heart (*18,20*) and also in cardiac ^{201}Tl studies (*11,21*). A recent study also demonstrated the accuracy of this approach in a combined SPECT/CT system (*22*). By incorporating a correction for collimator septal penetration by high-energy emissions, one can also make the technique applicable to ^{123}I (*19*).

The QSPECT reconstruction approach has estimated CBF images at rest in a clinical setting (*11*) and quantified CVR by measuring CBF at rest and after vasodilation in a single SPECT session. This was accomplished by using the dual-table autoradiographic (DTARG) method and a dual administration of ^{123}I-iodoamphetamine (*23*). In those studies, corrections for attenuation and scatter appeared to be essential for generating quantitative CBF maps that were consistent with those generated by ^{15}O-water PET (*11,23*).

These studies were, however, validated in a single institution using a limited range of SPECT systems, and the general applicability of this technique for different SPECT systems had yet to be fully established. Thus, the aim of this study was to verify that analysis of data with a standardized reconstruction package incorporating attenuation and scatter correction can provide reproducible results across multiple institutions for quantitative rest and acetazolamide challenge CBF estimation from a single SPECT session.

MATERIALS AND METHODS

Institutions and Subjects

The 12 participating institutions were clinical centers and generally did not have scientific staff dedicated to nuclear medicine software or hardware development. Standard, vendor-supplied software was used for the collection of the studies, with unmodified scanners and collimators clinically used for brain studies. The acquired data were reconstructed with the program package developed for this project. Manufacturers and models of camera systems and the number of detectors and collimators (including fanbeam or parallel hole) used by the institution are listed in Supplemental Table 1 (supplemental materials are available online only at http://jnm.snmjournals.org). All institutions performed experiments on physical phantoms according to the protocol described in the "Phantom Experiment" section. Of the 12 institutions, 9 obtained patient scans, whereas the remaining 3 provided only phantom data. Clinical studies were approved by institutions' ethics committees or followed guidelines for clinical research protocols authorized by the institution. All subjects at each institution gave written informed consent.

The clinical studies were divided into 3 protocols: intrainstitutional, intrasubject reproducibility (reproducibility); comparison with PET (vs. PET); and intrascan consistency of the dual-time-point split-dose (rest–rest). Studies were excluded from the analysis if there was severe patient motion during one of the studies or if there were changes in the condition of the patients between the first and second studies likely to lead to changes in CBF.

Eight institutions (institutions 1, 3, 4, 6, 8, 9, 11, and 12) participated in the reproducibility arm, in which quantitative CBF values measured on separate days were compared. In this arm, all patients experienced unilateral or bilateral stenosis or occlusion in the extracranial internal carotid artery. The patients' ages ranged from 43 to 81 y (mean ± SD, 65 ± 9 y). A total of 31 studies in this protocol were analyzed. Four patients had to be excluded from the analysis—2 because of significant changes in their pathophysiologic status between the studies and 2 because of severe motion and mispositioning in the scanner.

One institution (institution 4) performed the versus-PET studies. CBF values obtained by the DTARG method were compared with those by ^{15}O-water and PET. Studies were performed on 6 patients (5 men, 1 woman; age range, 71–74 y; mean age ± SD, 72 ± 1 y) with stenosis or occlusion of the extracranial internal carotid artery unilaterally (n = 3) or bilaterally (n = 3).

Two institutions (institutions 2 and 12) provided data for the rest–rest comparison. Five patients from institution 2 had chronic cerebral infarction, whereas 4 subjects from institution 12 had no sign of cerebral disease. Patients' ages ranged from 32 to 72 y (mean ± SD, 52 ± 15 y); 5 patients were men and 4 women.

Phantom Experiment

Three experiments were performed by each institution using the SPECT camera fitted with the collimators normally used in clinical brain studies. The first scan determined the absolute sensitivity or the becquerel calibration factor (BCF) of the reconstructed images. For 10 min, a 360° projection set was acquired of a syringe filled with a ^{123}I-iodoamphetamine solution of known radioactivity and placed at the center of the field of view. The syringe was supplied by Nihon-Medi Physics, and its radioactivity was calibrated to 111 MBq at noon on the day before the experiment, with an accuracy better than 3%, decaying to approximately 30 MBq at the time of the experiment, avoiding the dead time of the camera. The BCF was determined by dividing the absolute radioactivity by the total counts for the syringe region in the reconstructed image.

The second experiment determined the collimator septal penetration contribution (*24*) from high-energy photons into the primary 159-keV energy window for ^{123}I. A line-spread function was obtained from the projection data of a line source filled with ^{123}I-iodoamphetamine. The septal penetration was determined from the background level as described previously (*19*). A projection line-spread function was also generated from this line source placed in a water-filled cylindric phantom (diameter, 16 cm).

The third experiment used a 16-cm-diameter, 15-cm-long uniform cylindric phantom. The whole radioactivity used for the BCF determination was diluted into the phantom, and projection data were acquired for 30 min, using the clinical scan protocols described in the "Clinical Studies" section. The radioactivity concentration (counting rate per unit mass) of an approximately 0.3-mL sample from the phantom was measured using the well counters available at the various institutions. Both NaI- and plastic scintillator–based well counters were used (Supplemental Table

1). Average pixel counts derived from regions of interest on the reconstructed emission images were referred to the well counter radioactivity counting rate, to determine the cross-calibration factor between the SPECT images and well counter system. This cross-calibration factor was subsequently used for the blood sample counts of the clinical studies. Uniformity of the reconstructed emission images was evaluated.

Clinical Studies

All clinical SPECT studies followed the DTARG protocol, with dual administration of iodoamphetamine (*23*), depicted in Figure 1. Briefly, 2 dynamic scans were acquired in quick succession, with a 2-min interval between the scans. The first scan covered the initial 0- to 28-min period, and the second was acquired from 30 to 58 min. At 4 min per frame, 7 frames covered each of the 2 dynamic scan periods. ^{123}I-iodoamphetamine (111 MBq at institutions 2–12 or 167 MBq at institution 1) was infused twice over 1 min into the antecubital vein at 0 and 30 min. Acetazolamide (17 mg/kg, 1,000 mg maximum) was administered intravenously at 20 min after the first iodoamphetamine injection, corresponding to 10 min before the second iodoamphetamine injection. Projection data were summed for the acquisition duration of the first and second scans and reconstructed as described in the "QSPECT Reconstruction" section. In contrast to the study of Kim et al. (*23*), which used full arterial blood sampling, the individual arterial input functions were derived from a population-based standardized input function scaled with the whole-blood counts from a single arterial blood sample taken at approximately 10 min (*1,25–28*). This sample was also used for arterial blood gas analysis.

In the reproducibility arm, an additional, non-DTARG CBF study was performed on a separate day. Instead of DTARG, the previously reported ^{123}I-IMP autoradiographic (IMPARG) method (*1,19,25*) was performed within a month of the DTARG study. The IMPARG method is essentially equivalent to the present DTARG method, except that the IMPARG method uses a single iodoamphetamine administration to assess CBF either at rest or after acetazolamide challenge. The same image reconstruction process as for the DTARG protocol was used. In 12 studies, the DTARG protocol was used instead of IMPARG—namely, the DTARG study was performed twice to assess the CBF reproducibility at rest and after acetazolamide.

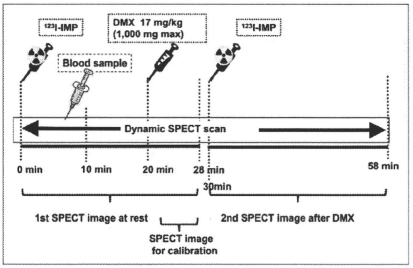

FIGURE 1. Scanning protocol flow for DTARG procedure. ^{123}I-iodoamphetamine was injected at 0 min, and 28-min resting dynamic SPECT scan was commenced. Blood sample for calibration of population input function was drawn at 10 min. Acetazolamide (DMX-diamox) was administered at 20 min. CBF values are scaled by last frame (time, 24–28 min). Second dynamic SPECT scan followed second injection of ^{123}I-iodoamphetamine at 30 min. IMP = iodoamphetamine.

In the versus-PET protocol, the PET study was performed within 2 d of the DTARG SPECT study. PET scans used intravenous ^{15}O-water both at rest and after the acetazolamide challenge. CBF images were calculated by the ^{15}O-water autoradiography technique (*29*), with careful corrections for delay and dispersion (*30–32*). Patients were stable between the SPECT and PET studies.

In the rest–rest protocol, the DTARG scan was obtained without the pharmacologic challenge during the study to evaluate the consistency of CBF values estimated from the 2 scans.

QSPECT Reconstruction

The program package for QSPECT uses a wrapper written in JAVA to run several programs written in C for Microsoft Windows systems. The package includes programs for reconstructing SPECT images, calculating functional images, coregistering images, and reslicing and printing summary logs.

The QSPECT package reconstructs images from the original projection data from commercial SPECT equipment, based on previous work by Iida and his colleagues (*19–21,23,33,34*). Reconstructed SPECT images are calibrated in Bq/mL, which provides independence from scanning parameters such as the acquisition time, number of views, matrix size, and zoom factor. Uniformity and center-of-rotation corrections and fanbeam–to–parallel beam conversion (for fanbeam collimators) were performed using the clinical routine software before reconstruction by this package.

An overall flow diagram of the correction and reconstruction process is shown in Supplemental Figure 1. The OSEM reconstruction technique includes attenuation correction (*17*). A threshold-based edge-detection algorithm generated the attenuation μ-map, assuming a uniform attenuation coefficient of 0.166 cm^{-1} for ^{99m}Tc (0.160 cm^{-1} for ^{123}I) as an average over the brain and skull (*19*). The threshold was optimized via the user interface to correctly define the brain outline. The attenuation μ-map was generated from the summed 0- to 28-min rest frame and was coregistered to the other images (*35*) reconstructed with filtered backprojection without attenuation or scatter correction. The attenuation μ-maps were forward projected to provide the transmission projection data for TDCS. The emission projections were scatter-corrected by the TDCS method, as originally proposed by Meikle et al. (*18*), and further optimized for realistic ^{99m}Tc, ^{201}Tl, and ^{123}I data in the brain and thorax regions (*20,21,23,33,34*). An offset compensated for the septal penetration of high-energy photons for ^{123}I studies, which adds fairly uniform background counts, or direct current (DC) components, to the projections.

Scatter- and attenuation-corrected images were reconstructed with OSEM (5 iterations, 5 subsets using geometric-mean projections, postreconstruction gaussian filter of 7 mm in full width at half maximum) and then realigned to the image set obtained from the first scan. The acquisition parameters and BCF were used to convert the reconstructed raw counts to Bq/mL.

The global CBF over the entire gray matter was estimated from the SPECT frame covering 24–28 min, because this timing minimizes the individual shape variations in individual input function. The look-up table generated for estimating CBF images from the complete dynamic study (0–28 min) was then

scaled to provide global cortical gray matter CBF values consistent with the 24- to 28-min frame estimates. A careful detection algorithm was used to reliably exclude extracranial accumulation of ^{123}I-iodoamphetamine (e.g., in the parotid region), which could adversely affect this scaling procedure. The regional CBF was then estimated at each pixel by means of the table look-up procedure (*25,28*). The background image at the time of the second ^{123}I-iodoamphetamine injection was estimated from the first-phase CBF images, according to the compartment model assumed in this study (*23*). An additional table look-up procedure was applied to the second dynamic dataset (30–58 min) for calculating the vasodilated (acetazolamide challenge) CBF images as described previously (*23*). The data were successfully reconstructed, and CBF was estimated at each institution. To facilitate and provide consistent analysis, the data presented are from the reanalysis conducted at the core lab (National Cerebral and Cardiovascular Center).

Data Analysis

The uniform phantom SPECT activity estimates were compared with the known activity in the phantom. Images for the baseline study were displayed with subsequent images using an absolute flow value scale to visually ascertain regional and global differences in flow. Regions of interest were placed on the middle cerebral artery territories of both hemispheres, and the average flow values between the different methods were compared and plotted. Bland–Altman plots and the SD of the differences evaluated the consistency of CBF values obtained from the reproducibility and versus-PET protocols.

All data were presented as mean ± SD. Pearson correlation analysis and linear regression analysis were used to evaluate relationships between the 2 CBF values. A P value less than 0.05 was considered statistically significant.

RESULTS

Phantom Studies

In the 16-cm scattering cylinder line source experiment, the scatter-uncorrected images show background counts extending beyond the phantom, from septal penetration of the high-energy photons. The scatter correction is largely effective in correcting for scatter and septal penetration counts. As shown in Supplemental Figure 2, the Toshiba-ECAM low- to medium-energy general-purpose (LMEGP) collimator, designed for reduced ^{123}I septal penetration, compared with the standard low-energy high-resolution collimator (GE Healthcare), demonstrates reduced scatter and septal penetration counts. The lower septal penetration of the Toshiba-ECAM LMEGP collimators is also supported by a lowered scatter correction offset value (DC = 0.05, compared with DC = 0.20 for the GE low-energy high-resolution collimator). The reduced scatter and septal penetration result in more complete removal of scatter for the LMEGP collimator.

Figure 2 displays reconstructed slices of the uniform phantom for all 12 institutions, scaled to the same maximum activity concentration. The estimated activity concentrations from these studies, compared with the known activity concentration, represented an accuracy of 87.5% ± 5.1% (Supplemental Table 1). The well counter–to–SPECT cross-calibration factor, which represents the sensitivity of the well counter system for ^{123}I, was 0.5–1.0 for NaI systems and 0.1–0.2 for plastic scintillation detector systems. The BCF values were consistent for the same SPECT camera–collimator configurations.

Clinical Studies

Figure 3A shows typical CBF images obtained at 4 institutions with 4 different γ-camera vendors, performed as part of the reproducibility arm of the study. Each case shows different CBF distributions both at rest and after acetazolamide challenge. The acetazolamide images obtained using the DTARG method agree well with the images subsequently obtained with the IMPARG method after acetazolamide infusion.

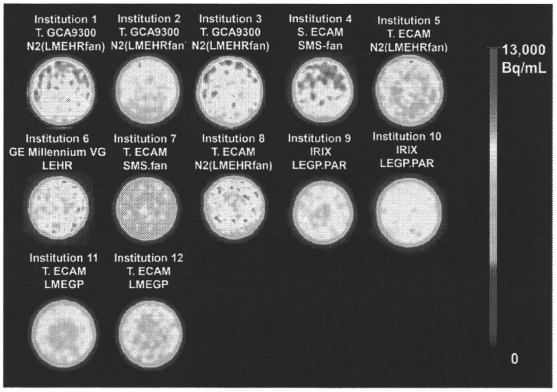

FIGURE 2. Reconstructed slices through uniform phantom from the participating 12 institutions. Experiment was designed to have same phantom activity concentration for each center's study. Nonuniformities and also differences in absolute activity concentration estimates can be observed, highlighting need for rigorous calibration, flood correction, and quality control. Legend above each image gives institution number (given in Supplemental Table 1), γ-camera model, and collimator used.

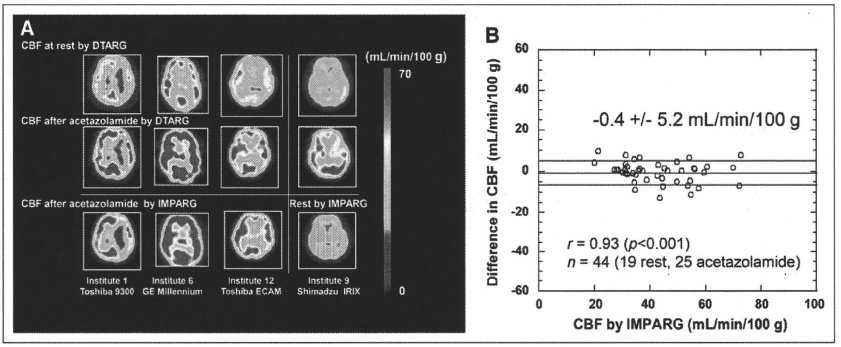

FIGURE 3. (A) Images from reproducibility study. CBF images obtained at rest and after acetazolamide with DTARG method. Repeated scan (third row) within 1 mo using IMPARG method and acetazolamide stress (columns 1–3) and at rest (last column). Images demonstrate that CVR can be estimated with this technique and demonstrate good reproducibility of measuring both at rest and after acetazolamide challenge CBF. (B) Bland–Altman plot showing difference vs. IMPARG CBF values estimated from DTARG method and repeated IMPARG studies to assess reproducibility. Little systematic bias is detected (mean difference, −0.4 mL/100 g/min), and SD of differences is moderate (5.2 mL/100 g/min). Correlation coefficient of $r = 0.93$ ($P < 0.001$) was found.

CBF images of a subject with left middle cerebral artery occlusion are shown in Supplemental Figure 3 for slices covering the whole brain. The images demonstrate reduced CBF after acetazolamide challenge in the left middle cerebral artery territory. The good reproducibility is confirmed by the Bland–Altman plot comparison of DTARG CBF values, with the CBF values obtained at a different imaging session with IMPARG or DTARG (Fig. 3B). The SD of the differences is 5.2 mL/100 g/min, with low bias supported by the mean difference of 0.4 mL/100 g/min. Regression analysis between DTARG and IMPARG values yielded a significant correlation ($P < 0.001$), with a correlation coefficient of $r = 0.93$.

Figure 4A shows MR and CBF images at rest and after acetazolamine obtained with DTARG SPECT and ^{15}O-water PET in a 73-y-old male patient (63 kg) with right internal carotid artery occlusion and left internal carotid stenosis. The MR images do not show any evidence of cerebral infarction in either hemisphere. Rest CBF was reduced bilaterally in the frontal-to-parietal regions, and acetazolamide increased CBF in left parietal regions but not in the right parietal area. DTARG CBF indicated the loss of vasoreactivity in the right internal carotid artery stenotic area. These findings were consistent with those from the PET evaluation. An additional example is shown in Supplemental Figure 4 for a 74-y-old female patient (48 kg) with left internal carotid artery stenosis, for whom MR images did not show cerebral infarction. DTARG CBF demonstrated preserved CBF in both hemispheres but reduced CBF reactivity in the left middle cerebral artery territory. The findings were again consistent with those from PET. Figure 4B compares the flow values obtained at rest and after acetazolamide with DTARG with the corresponding values obtained by ^{15}O-water PET. The SD of the differences is 5.1 mL/100 g/min, with the significant underestimation by ^{15}O-water PET, compared with PET by the DTARG method, highlighted by a mean difference of −6.1 mL/100 g/min. The Pearson analysis showed a significant correlation ($P < 0.001$), with a correlation coefficient of $r = 0.88$.

The results from the rest–rest protocol are summarized in Figure 5. The differences between the measurements performed with the 2 injections were small, with good agreement between the 2 flow values. The mean ± SD of the differences was 0.6 ± 2.9 mL/100 g/min.

DISCUSSION

The QSPECT package provided quantitative images consistent between the participating centers, using dual- or triple-detector SPECT scanners and collimators routinely used for nonquantitative brain studies. All centers successfully acquired the dynamic SPECT images, and the data from the variety of cameras encountered were successfully processed by the software package. Rest CBF and CVR could be readily obtained by the participating institutions in a single, clinically practical, 1-h scanning session. Good reproducibility of CBF estimates was observed in 31 pairs of studies at 8 institutions (Fig. 3), and the CBF estimated with the ^{123}I-iodoamphetamine SPECT agreed well with ^{15}O-water PET CBF at 1 institution (Fig. 4). The CBF values after the second injection of the DTARG were consistent with the values obtained after the

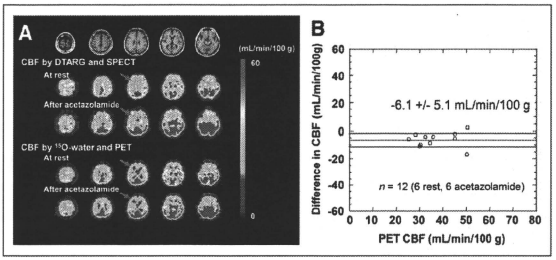

FIGURE 4. (A) MR and CBF images at rest and after acetazolamide stress assessed with corresponding measurements with ^{15}O-water PET (vs. PET evaluation) in patient with right internal carotid artery occlusion and left internal carotid stenosis. Gaussian filter was not applied to SPECT CBF in this display. (B) Bland–Altman plot. Moderate underestimation of CBF determined by DTARG method, compared with PET, is observed (mean difference, −6.1 mL/100 g/min). Correlation coefficient of $r = 0.88$ ($P < 0.001$) was found.

first injection when no vasodilating stress was given in 9 studies at 2 institutions (Fig. 5).

Quantitative CBF and CVR in response to acetazolamide challenge can be of significant prognostic value for patients considered for revascularization of cerebral arteries (*5–7*). The previously validated IMPARG method requires 2 independent scans on different days to assess the CVR (*5–7*), limiting it for routine clinical studies. The DTARG protocol to quantitatively assess CBF both at rest and after acetazolamide from a single dynamic SPECT session with the dual administration of ^{123}I-iodoamphetamine (*23*) facilitates clinical use. Errors caused by ambiguity in the absolute scaling, and possible changes in physiologic status of the subjects between scans, can be reduced substantially with the DTARG protocol. The quantitative reconstruction program enabled the compartment model–based kinetic analysis to compensate for the residual radioactivity concentration during the second session of the dynamic scan.

Major error sources in SPECT, namely attenuation and scatter, are only object-dependent (*14*) and not γ-camera– or collimator-dependent, and thus SPECT images obtained by this quantitative reconstruction package should be consistent across systems. Septal penetration of high-energy photons for ^{123}I is, however, collimator-dependent (*24*) but could be compensated as part of the TDCS scatter correction algorithm (*11*), as demonstrated in Supplemental Figure 2. The radioactivity concentration of the uniform cylinder phantom estimated in units of Bq/mL was consistent and showed variation within ±5.1% (Fig. 2; Supplemental Table 1), though a systematic underestimation by 12.5%, which is attributed to the BCFs being derived from a line source in air, reconstructed without scatter, attenuation, and septal penetration corrections. However, this underestimation does not affect the CBF estimation, because it relies on the direct cross-calibration between the γ-counter used to count the blood sample and the SPECT measurements.

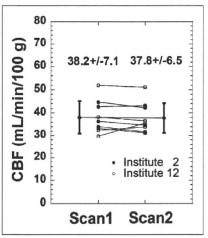

FIGURE 5. Results from rest–rest evaluation carried out at 2 institutions (2 and 12). In this study, DTARG method was performed as per normal protocol but without pharmacologic stress. CBFs estimated with first injection (left on graph) are in good agreement with those estimated after second injection (right on graph).

This phantom study also highlighted the importance of proper calibration and quality control of the γ-camera to avoid artifacts and bias in the reconstructed images. These corrections were applied, as for other clinical studies, by the vendors' software rather than as part of the QSPECT system, because these corrections are typically performed online and on-the-fly, with only the corrected data being stored. The nonuniformities seen on some phantom images should improve with more rigorous quality-control procedures.

The previously validated population-based input function requiring only a single arterial blood sample for scaling (*1,25–28*) has been incorporated in the software package. Blood from this single arterial sample is also used to measure arterial blood gases, which are relevant and of interest clinically in these patients. The timing of the single blood sample (~10 min after iodoamphetamine injection) was optimized previously (*1,25–28*) to minimize the errors associated with individual differences in shape of the arterial input function. In addition, absolute global CBF was estimated from SPECT images taken at an optimized mid scan time of approximately 30 min (24–28 min), rather than from the initial part of the study, to maximize the accuracy of using the population-based input function (*1,25–28*).

Partial-volume correction has not been implemented as part of this processing protocol. Partial-volume effects can potentially lead to underestimation of flow values in gray matter regions because of the limited resolution of SPECT. The small underestimation of 6.1 mL/100 g/min by the DTARG method, compared with ^{15}O-water PET (Fig. 4B), is attributed to the partial-volume effects due to differences in resolution between PET and SPECT. The underestimation can also lead to variations in CBF values obtained with different-

resolution collimators. However, consistent postreconstruction filtering, as applied in this study, can reduce this effect.

Only the reproducibility within an institution was assessed. Hence, the reproducibility of measurements between institutions cannot be gleaned from these data, particularly because patients with vascular disease were studied. Thus, unlike estimates from healthy volunteers, flow values and vascular reactivity are expected to vary from patient to patient, and flow values determined at one institution with one group of patients are therefore not directly comparable with flow values from another group of patients in another institution. A realistic brain phantom, such as recently developed by our group, simulating head contour with bone attenuation, could be used to assess the consistency of brain images between institutions.

CONCLUSION

The developed QSPECT package allows absolute CBF and CVR to be estimated in routine clinical studies. This multicenter study has demonstrated the applicability of QSPECT for a variety of clinical settings and equipment. Results from the studies suggest that a change of approximately 10% or 5 mL/min/100 g can be readily detected in follow-up studies. The graphical user interface for easily controlling the in-built sophisticated programs and tools ensures that routine use does not require dedicated support from scientific or computing staff. The package is now successfully used in over 130 institutions in Japan, and more than 25,000 patient studies have been analyzed with the QSPECT package.

ACKNOWLEDGMENTS

We thank the staff of each of the following institutions that participated in this project for their invaluable help with supporting the SPECT studies: Azabu Neurosurgical Hospital, Sapporo City; Asahikawa Red Cross Hospital, Asahikawa City; Handa City Hospital, Handa City; Ichinomiya Municipal Hospital, Ichinomiya City; Kashiwaba Neurosurgical Hospital, Sapporo City; Japanese Red Cross Kobe Hospital, Kobe City; Nakamura Memorial Hospital, Sapporo City; National Cardiovascular Center, Osaka; Ogori Daiichi General Hospital, Yamaguchi City; Oji General Hospital, Tomakomai City; Sunagawa City Medical Center, Sunagawa City; and Teine Keijinkai Hospital, Sapporo City. The present study was supported by the Japan Cardiovascular Research Foundation and a grant for Translational Research from the Ministry of Health, Labor and Welfare (MHLW), Japan.

REFERENCES

1. Iida H, Akutsu T, Endo K, et al. A multicenter validation of regional cerebral blood flow quantitation using [^{123}I]iodoamphetamine and single photon emission computed tomography. *J Cereb Blood Flow Metab.* 1996;16:781–793.
2. Hatazawa J, Iida H, Shimosegawa E, Sato T, Murakami M, Miura Y. Regional cerebral blood flow measurement with iodine-123-IMP autoradiography: normal values, reproducibility and sensitivity to hypoperfusion. *J Nucl Med.* 1997;38:1102–1108.
3. Yamaguchi T, Kanno I, Uemura K, et al. Reduction in regional cerebral metabolic rate of oxygen during human aging. *Stroke.* 1986;17:1220–1228.
4. Ogasawara K, Ito H, Sasoh M, et al. Quantitative measurement of regional cerebrovascular reactivity to acetazolamide using ^{123}I-*N*-isopropyl-*p*-iodoamphetamine autoradiography with SPECT: validation study using $H_2{}^{15}O$ with PET. *J Nucl Med.* 2003;44:520–525.
5. Ogasawara K, Ogawa A, Terasaki K, Shimizu H, Tominaga T, Yoshimoto T. Use of cerebrovascular reactivity in patients with symptomatic major cerebral artery occlusion to predict 5-year outcome: comparison of xenon-133 and iodine-123-IMP single-photon emission computed tomography. *J Cereb Blood Flow Metab.* 2002;22:1142–1148.
6. Ogasawara K, Ogawa A, Yoshimoto T. Cerebrovascular reactivity to acetazolamide and outcome in patients with symptomatic internal carotid or middle cerebral artery occlusion: a xenon-133 single-photon emission computed tomography study. *Stroke.* 2002;33:1857–1862.
7. Ogasawara K, Ogawa A. JET study (Japanese EC-IC Bypass Trial) [in Japanese]. *Nippon Rinsho.* 2006;64(suppl 7):524–527.
8. Fujita M, Ichise M, Zoghbi SS, et al. Widespread decrease of nicotinic acetylcholine receptors in Parkinson's disease. *Ann Neurol.* 2006;59:174–177.
9. Deloar HM, Watabe H, Kudomi N, Kim KM, Aoi T, Iida H. Dependency of energy and spatial distributions of photons on edge of object in brain SPECT. *Ann Nucl Med.* 2003;17:99–106.
10. Iida H, Eberl S, Kim KM, et al. Absolute quantitation of myocardial blood flow with ^{201}Tl and dynamic SPECT in canine: optimisation and validation of kinetic modelling. *Eur J Nucl Med Mol Imaging.* 2008;35:896–905.
11. Iida H, Eberl S. Quantitative assessment of regional myocardial blood flow with thallium-201 and SPECT. *J Nucl Cardiol.* 1998;5:313–331.
12. Eberl S, Chan HK, Daviskas E, Constable C, Young I. Aerosol deposition and clearance measurement: a novel technique using dynamic SPET. *Eur J Nucl Med.* 2001;28:1365–1372.
13. Hapdey S, Soret M, Ferrer L. Quantification in SPECT: myth or reality? A multicentric study. *IEEE Nucl Sci Symp Conf Rec.* 2004;5:3170–3317.
14. Graham LS, Fahey FH, Madsen MT, van Aswegen A, Yester MV. Quantitation of SPECT performance: report of Task Group 4, Nuclear Medicine Committee. *Med Phys.* 1995;22:401–409.
15. Hendel RC, Corbett JR, Cullom SJ, DePuey EG, Garcia EV, Bateman TM. The value and practice of attenuation correction for myocardial perfusion SPECT imaging: a joint position statement from the American Society of Nuclear Cardiology and the Society of Nuclear Medicine. *J Nucl Cardiol.* 2002;9:135–143.
16. Zaidi H, Koral KF. Scatter modelling and compensation in emission tomography. *Eur J Nucl Med Mol Imaging.* 2004;31:761–782.
17. Hudson HM, Larkin RS. Accelerated image reconstruction using ordered subsets of projection data. *IEEE Trans Med Imaging.* 1994;13:601–609.
18. Meikle SR, Hutton BF, Bailey DL. A transmission-dependent method for scatter correction in SPECT. *J Nucl Med.* 1994;35:360–367.
19. Iida H, Narita Y, Kado H, et al. Effects of scatter and attenuation correction on quantitative assessment of regional cerebral blood flow with SPECT. *J Nucl Med.* 1998;39:181–189.
20. Narita Y, Eberl S, Iida H, et al. Monte Carlo and experimental evaluation of accuracy and noise properties of two scatter correction methods for SPECT. *Phys Med Biol.* 1996;41:2481–2496.
21. Narita Y, Iida H, Eberl S, Nakamura T. Monte Carlo evaluation of accuracy and noise properties of two scatter correction methods for ^{201}Tl cardiac SPECT. *IEEE Trans Nucl Sci.* 1997;44:2465–2472.
22. Willowson K, Bailey DL, Baldock C. Quantitative SPECT reconstruction using CT-derived corrections. *Phys Med Biol.* 2008;53:3099–3112.
23. Kim K, Watabe H, Hayashi T, et al. Quantitative mapping of basal and vasareactive cerebral blood flow using split-dose ^{123}I-idoamphetamine and single photon emission computed tomography. *Neuroimage.* 2006;33:1126–1135.
24. Kim KM, Watabe H, Shidahara M, Ishida Y, Iida H. SPECT collimator dependency of scatter and validation of transmission dependent scatter compensation methodologies. *IEEE Trans Nucl Sci.* 2001;48:689–696.
25. Iida H, Itoh H, Nakazawa M, et al. Quantitative mapping of regional cerebral blood flow using iodine-123-IMP and SPECT. *J Nucl Med.* 1994;35:2019–2030.
26. Iida H, Nakazawa M, Uemura K. Quantitation of regional cerebral blood flow using 123I-IMP from a single SPECT scan and a single blood sampling: analysis on statistical error source and optimal scan time [in Japanese]. *Kaku Igaku.* 1995;32:263–270.
27. Kurisu R, Ogura T, Takikawa S, Saito H, Nakazawa M, Iida H. Estimation and optimization of the use of standard arterial input function for split-dose administration of *N*-isopropyl-*p*[^{123}I]iodoamphetamine [in Japanese]. *Kaku Igaku.* 2002;39:13–20.

28. Ogura T, Takikawa S, Saito H, Nakazawa M, Shidahara M, Iida H. Validation and optimization of the use of standardized arterial input function in *N*-isopropyl-*p*[^{123}I]iodoamphetamine cerebral blood flow SPECT [in Japanese]. *Kaku Igaku.* 1999;36:879–890.
29. Shidahara M, Watabe H, Kim KM, et al. Evaluation of a commercial PET tomograph-based system for the quantitative assessment of rCBF, rOEF and $rCMRO_2$ by using sequential administration of ^{15}O-labeled compounds. *Ann Nucl Med.* 2002;16:317–327.
30. Iida H, Higano S, Tomura N, et al. Evaluation of regional differences of tracer appearance time in cerebral tissues using [^{15}O] water and dynamic positron emission tomography. *J Cereb Blood Flow Metab.* 1988;8:285–288.
31. Iida H, Kanno I, Miura S, Murakami M, Takahashi K, Uemura K. Error analysis of a quantitative cerebral blood flow measurement using $H_2{}^{15}O$ autoradiography and positron emission tomography, with respect to the dispersion of the input function. *J Cereb Blood Flow Metab.* 1986;6:536–545.
32. Iida H, Kanno I, Miura S, Murakami M, Takahashi K, Uemura K. A determination of the regional brain/blood partition coefficient of water using dynamic positron emission tomography. *J Cereb Blood Flow Metab.* 1989;9:874–885.
33. Iida H, Shoji Y, Sugawara S, et al. Design and experimental validation of a quantitative myocardial ^{201}Tl SPECT System. *IEEE Trans Nucl Sci.* 1999;46:720–726.
34. Narita Y, Iida H. Scatter correction in myocardial thallium SPECT: needs for optimization of energy window settings in the energy window-based scatter correction techniques [in Japanese]. *Kaku Igaku.* 1999;36:83–90.
35. Eberl S, Kanno I, Fulton RR, Ryan A, Hutton BF, Fulham MJ. Automated interstudy image registration technique for SPECT and PET. *J Nucl Med.* 1996;37:137–145.

社団法人 電子情報通信学会
THE INSTITUTE OF ELECTRONICS,
INFORMATION AND COMMUNICATION ENGINEERS

信学技報
IEICE Technical Report

コリメータ開口補正およびモンテカルロ法に基づく散乱線補正を用いたSPECT画像再構成の定量精度評価

崎本 智則[†a)]　銭谷 勉[‡]　渡部 浩司[‡*]　Antti Sohlberg[‡]　石田 健二[‡]

平野 祥之[‡]　湊 小太郎[†]　飯田 秀博[‡]

†奈良先端科学技術大学院大学情報科学研究科 〒630-0193 奈良県生駒市高山町 8395-5
‡国立循環器病センター研究所先進医工学センター放射線医学部 〒565-8565 大阪府吹田市藤白台 5-7-1
*大阪大学大学院医学系研究科 〒565-0871 大阪府吹田市山田丘 2-2

a)E-mail: tomonori-s@is.naist.jp

あらまし 近年，我々はコリメータ開口補正による解像度補正，吸収補正，モンテカルロ法に基づいた散乱線補正機構を搭載した画像再構成法を開発してきた．本研究では，^{99m}Tc溶液で満たされた一連のファントム実験を行い，本画像再構成法の定量精度を検証した．東芝製SPECT装置GCA7200Aを用いて，線線源ファントムによる空間解像度の評価，ピラミッドファントム，偏心リングファントムおよび脳ファントムによる定量性の評価を行った．実験の結果，本手法の吸収補正と散乱線補正の妥当性が確認できた．また，コリメータ開口補正は解像度を大きく改善しただけでなく，部分容積効果改善および統計雑音抑制効果もあり，大きな利点と考えられた．本手法は局所機能画像定量SPECTに貢献することが期待される．

キーワード SPECT，画像再構成，定量性，散乱線補正，モンテカルロ法，コリメータ開口補正

Evaluation of Quantitative Accuracy of a Novel Image Reconstruction of SPECT with Monte Carlo-Based Scatter Compensation and Collimator Blurring Compensation

Tomonori SAKIMOTO[†a)]　Tsutomu ZENIYA[‡]　Hiroshi WATABE[‡*]　Antti SOHLBERG[‡]

Kenji ISHIDA[‡]　Yoshiyuki HIRANO[‡]　Kotaro MINATO[†]　and　Hidehiro IIDA[‡]

† Graduate School of Information Science, Nara Institute of Science and Technology 8395-5 Takayama-cho, Ikoma-shi, Nara, 630-0193 Japan
‡ Department of Investigative Radiology, Advanced Medical Engineering Center, National Cardiovascular Center Research Institute 5-7-1 Fujishirodai, Suita-shi, Osaka, 565-8565 Japan
*Graduate School of Medicine, Osaka University 2-2 Yamadaoka, Suita-shi, Osaka, 565-0871 Japan

a)E-mail: tomonori-s@is.naist.jp

Abstract Recently we developed a novel SPECT image reconstruction method that includes attenuation compensation (AC), collimator-detector response compensation (CDRC) and Monte Carlo-based scatter compensation (MCSC). The aim of this study was to quantitatively evaluate our reconstruction method for brain SPECT by phantom experiments with ^{99m}Tc. We performed the following experiments using a SPECT camera with LEHR parallel-hole collimator (GCA-7200A, Toshiba, Japan): (1) measurement of spatial resolution with line sources, (2) evaluation of quantitaion with pyramid phantom, eccentric ring phantom, 2D brain phantom and 3D phantom. These results suggested that our reconstruction algorithm with AC, MCSC and CDRC was valid to improve resolution and quantitation in brain SPECT.

Keyword SPECT, image reconstruction, quantitation, scatter compensation, Monte Carlo, collimator-detector response compensation

1. はじめに

SPECT(single photon emission computed tomography)では，コリメータの開口によって空間解像度が低下する．また，被写体内でのガンマ線の吸収および散乱によって，定量性が低下する．

我々は，吸収補正(attenuation compensation; AC)，コリメータ開口補正(collimator-detector response compensation; CDRC)，モンテカルロ法に基づく散乱線補正(Monte Carlo-based scatter compensation; MCSC)を組み込んだ画像再構成法を開発した[1]．本研究では，我々が開発した画像再構成法の実用化を目指し，一連の物理ファントム実験を行い，定量精度を検証した．

2. 方法

1) 画像再構成

本手法では，OS-EM(ordered subset expectation maximization)法[2]を画像再構成に用い，順投影部分に散乱線分布を加えることにより散乱線補正を行った．順投影部分に散乱線分布を加えた OS-EM 法の漸化式は，式(1)のように表わされる．

$$\lambda_j^{new} = \frac{\lambda_j^{old}}{\sum_{i\in S_n} a_{ij}} \sum_{i\in S_n} \frac{a_{ij} y_i}{\sum_k a_{ik}\lambda_k^{old} + s_i} \quad (1)$$

ここで j および k は再構成画素の通し番号，i は検出器画素の通し番号，a_{ij} は画素 j から放出されたガンマ線が検出器 i で検出される確率，y は計測により得た投影データ，λ は再構成画像，s は散乱線投影分布である．吸収補正およびコリメータ開口補正は，以下に述べるように，検出確率 a_{ij} に吸収およびコリメータ応答のモデルを組み込むことにより実装された．また本手法では，吸収，散乱，コリメータ開口の各補正を簡単に実装するために，画像マトリクスを回転してから順投影および逆投影を行う Rotation-based 法[3]を用いた．

2) コリメータ開口補正

SPECT ガンマカメラの分解能は検出器の固有分解能およびコリメータ特性により決定される．一般に，パラレルホールコリメータにおけるコリメータ応答関数(collimator-detector response function: CDRF)は二次元のガウシアン関数とみなすことができる．また，コリメータ応答関数の半値幅(full width at half maximum: FWHM)は，検出器と線源との間の距離に比例して直線的に大きくなると仮定できるので，

$$FWHM(d) = \alpha d + \beta \quad (2)$$

で表わすことができる[4]．ここで d は検出器と線源の間の距離である．α と β の値を実験的に求めることにより，コリメータ応答関数は線源と検出器の距離に依存した線形モデルとして表すことができる．

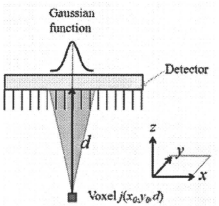

Fig.1 コリメータ応答関数

Fig.1 で示すように変数を定義したとき，コリメータ応答関数は，

$$h(x,y,d) = \frac{1}{2\pi\sigma^2(d)} \exp\left(-\frac{r^2}{2\sigma^2(d)}\right) \quad (3)$$

と表される．ここで σ はガウシアン関数の標準偏差で，ガウシアン関数の半値幅の約 0.425 倍となる．r は (x_0,y_0) と (x,y) との間の距離である．

コリメータ応答関数を考慮したとき，画素 $j(x_0,y_0,d)$ から放出されたガンマ線が検出器 $i(x,y)$ に検出される確率は，

$$a_{ij} = \frac{h(x,y,d)}{\sum_r h(x,y,d)} \quad (4)$$

となる．検出確率を式(4)により導出し，画像再構成において検出確率として用いることにより，コリメータ開口補正を実装できる[5,6]．

3) 吸収補正

式(5)に示すように吸収の影響を検出確率に組み込むことにより，吸収補正を行う．

$$a_{ij\_AC+} = a_{ij\_AC-} \cdot \exp\left(-\sum_{k\in L} \mu_k l\right) \quad (5)$$

ここで a_{ij_ac+} は吸収の影響を考慮した検出確率，a_{ij_ac-} は吸収の影響を考慮しない検出確率，L はガンマ線が放出された画素 j と検出器 i の間の経路，μ_k は画素 k における吸収係数[cm^{-1}]，l は，経路 L において，画素 k を通った距離である．

頭部は吸収係数分布の点から考えると，軟部組織と頭蓋骨の 2 つから成る単純な構造である．したがって，^{99m}Tc のエネルギーピーク 140keV においては，2 つの領域を考慮した均一な吸収係数 0.167 cm^{-1} を頭部の輪郭内に設定したものを吸収係数マップとして画像再構

成の検出確率に組み込むことで補正できる[7]. 輪郭抽出は, しばしば SPECT 投影データをフィルタ補正逆投影法(Filtered Back-Projection: FBP)で再構成した画像に対して, 閾値処理して行われるが, 本研究では大きさが既知のファントムを利用したので, 閾値処理した輪郭の大きさがファントムと同じになるように, 対話的に閾値を調整した. また, 輪郭の多少のずれは再構成結果にあまり影響しない[8].

4) モンテカルロ法に基づく散乱線補正

散乱線推定は, 画像再構成により得た推定像と吸収係数マップをモンテカルロ法における散乱体として利用する. 吸収係数マップは上述の吸収補正で使用するものと同様のものを使用する. 我々の開発した手法では, delta scattering algorithm[9,10], convolution-based forced detection (CFD)[11]を用いたモンテカルロ法により散乱線を推定している. また散乱線分布は低周波な画像であるという前提のもと, coarse grid[12]および intermittent scatter modeling[12]を利用して, 散乱線推定の計算時間を短縮した. coarse grid とは, 再構成画像および吸収係数マップをダウンサンプリングした画像を用いて散乱線推定を行い, 推定後に線形補間により元のサイズの画像に戻す手法である. また, intermittent scatter modeling とは, 逐次近似画像再構成において, 散乱線推定を最初の数回の反復でのみ行い, その後の反復では定数として扱う手法である.

本研究では 128×128×128 の原画像を 64×64×64 にダウンサンプリングして散乱線推定を行い, 2 回の反復で推定を打ち切った. また, モンテカルロ法のイベント数は, 1 投影あたり 10,000,000 回とした.

3. 実験

開発した画像再構成法を検証するために, 東芝製 SPECT 装置 GCA 7200-A および低エネルギー高解像度用パラレルホールコリメータ LEHR を用いて, 一連のファントム(複数線線源ファントム, ピラミッドファントム, 偏心リングファントム, 2D 脳ファントム, 3D 脳ファントム)の撮像を行った. 2D 脳ファントムおよび 3D 脳ファントムの頭蓋骨部分には, 吸収係数が骨とほぼ等しいリン酸水素カリウム溶液を封入した. **Fig.2** に, 本研究で用いたファントムおよび撮像時間, 線源の放射能を示す. 本研究では核種に ^{99m}Tc を用い, 収集エネルギーウインドウは 140keV±10%とした. ファントムは, 画像サイズ 128×128pixels, ピクセルサイズ 2.15×2.15mm^2, 回転半径 130mm, 投影データは 360 度に対して 90 投影で収集された. OS-EM 画像再構成の条件としては, サブセット数を 5 とし, 反復回数はコリメータ開口補正を行わない場合は 5 回, コリメータ開口補正を行う場合は 24 回とした. これは, コリメータ開口補正を行うことにより収束までに必要な反復回数が増加するためである.

1) 複数線線源ファントム

CDRC による解像度の改善を評価するために, 内径 0.9mm, 長さ 160mm のプラスチックチューブを ^{99m}Tc で満たした線線源で構成された複数線線源ファントム(**Fig.2**(a))を撮像した. 再構成画像上でそれぞれの線線源に対して, 二次元ガウシアン関数でフィッティングし, その半値幅により各線線源の解像度を評価した.

2) ピラミッドファントム

濃度一様の対象が, 物体の大きさに関わらず再構成画像において一様に描出されるかを確認するために, **Fig.2**(b)に示す直径の異なる円柱から構成されたピラミッドファントムを撮像した. あらかじめ測定したキャリブレーションファクター(再構成画像のボクセル値と放射能の間の比例定数)を再構成画像に乗じることにより, 放射能濃度分布画像を得た. 半径 25mm の円形の ROI(Region of Interest:関心領域)を各スライスにとり, 直径サイズに関わらず真の放射能濃度に近い値となるか, また, 濃度一様な画像が得られるかを評価した.

3) 偏心リングファントム

濃度一様の対象が, 偏った分布をしていても再構成画像において一様に描出されるかを確認するために, **Fig.2**(c)に示す偏心リングファントムを撮像した. 再構成画像のリング上に, 短軸 6mm, 長軸 30mm, 厚さ 120mm の楕円柱状の ROI を 4 か所とり, 位置に依存せず一様なカウントが得られるかを評価した.

4) 2D 脳ファントム

2D 脳ファントム(**Fig.2**(d))は白質領域と灰白質領域の放射能濃度比が 1:4 となるように設計されている. 画像再構成法の定量精度を評価するため, 再構成画像の白質領域と灰白質領域に複数の ROI をとり(**Fig.3**), 白質領域と灰白質領域の放射能濃度比を求め, 真の濃度比 1:4 と比較し, 定量精度を評価した.

5) 3D 脳ファントム

コリメータ開口補正モデルはガンマ線が検出器に真っすぐに入射する従来モデルと比べて, 解像度の改善だけでなく, 統計雑音抑制効果もあると言われる[5]. そこで, 本画像再構成法による統計雑音抑制効果を評価するため, 灰白質領域を ^{99m}Tc で満たした 3D 脳ファントム(**Fig.2**(e))を, 1 フレーム 10 分間で, 12 フレー

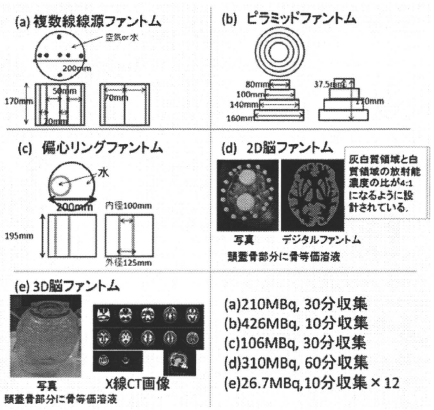

Fig.2 本研究で用いたファントム

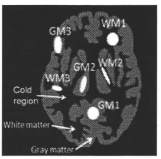

Fig.3 2D 脳ファントムに設定した ROI

ムを収集し，12 フレームそれぞれに対して，コリメータ開口補正有り/無しで OS-EM 画像再構成を行い，フレーム間の画素値の CoV(Coefficient of Variance; 100×標準偏差/平均[%]) を求め，CoV 画像を作成した．コリメータ開口補正を行わない場合は反復回数を 5 回とし，コリメータ開口補正を行った場合は反復回数を変化させて画像再構成し,各反復回数での CoV 画像を得た．また,複数線線源ファントム(水中)における，中央の線線源の FWHM を解像度の指標とし，これらから，コリメータ開口補正有り/無しにおける解像度と CoV の関係を調べた．CoV は 3D 脳ファントムの CoV 画像において視床および脳室に ROI をとり，その平均値をプロットした．さらに,コリメータ開口補正有りで,コリメータ開口補正無しの解像度と同程度の解像度となる反復回数を調べ,コリメータ開口補正有り/無しにおいて 3D 脳ファントム画像および CoV 画像を比較した．

4. 結果と考察

1) 解像度の評価

Fig.4 に，複数線線源ファントムの再構成画像および

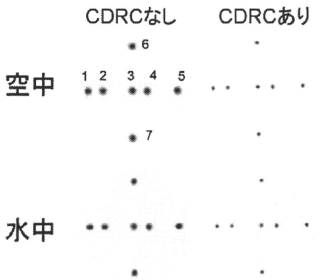

Fig.4 複数線線源ファントムの再構成画像

Table 1 複数線線源再構成画像の FWHM[mm]

	空中		水中	
線源番号	CDRC なし	CDRC あり	CDRC なし	CDRC あり
1	9.1	4.5	8.8	4.6
2	9.2	4.5	8.6	4.6
3	9.2	4.4	8.9	5.4
4	9.2	4.4	8.7	4.9
5	9.0	4.3	8.8	4.5
6	9.3	4.5	8.8	4.7
7	9.3	4.5	8.9	4.6

線源番号を示す．空中では AC と SC は無し、水中では AC と SC は有りとした．**Table 1** に，複数線線源ファントムの再構成画像における線線源の FWHM を示す．空中，水中ともに，すべての線源において，解像度が 4～5mm 程度改善した．

2) ピラミッドファントムと偏心リングファントムによる濃度一様性と定量性の評価

Fig.5 に，ピラミッドファントムのスライス毎の ROI 平均値のプロファイルを示す．AC,SC なしで再構成した場合，全体的に過小評価となり，特に円の径が大きいスライスで大きく過小評価となった．吸収の影響が大きかったと考えられる．AC のみ行って再構成した場合，全体的に過大評価となり，特に円の径が大きいスライスで大きく過大評価となった．散乱線の影響によると考えられる．AC と SC を行った場合，CDRC 有り無しともに，真値に近く，円の径に依存せず，ほぼ一様な値に再構成された．但し，CDRC を行った場合，エッジ付近で Gibbs-like artifact[13]が見られた．

Fig.6 に，偏心リングファントムの各 ROI における平均カウントの比を示す．カウントは，全 ROI 領域のピクセル値の平均により正規化した．Triple energy window (TEW)法により散乱線補正を行い，FBP で画像再構成し，Chang の方法で吸収補正をした場合，カウントが最大の領域と最少の領域の差が 26.5%程度あっ

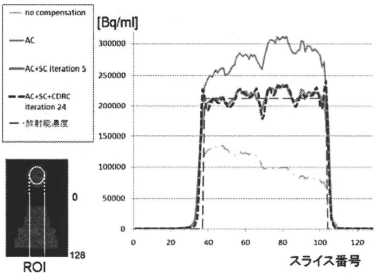

Fig.5 ピラミッドファントム ROI プロファイル

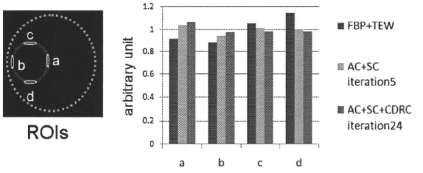

Fig.6 偏心リングファントム

たが，AC,SC を行った場合 9.6%，AC,SC,CDRC すべて行った場合 8.9%となり，線源が偏って分布した場合でも，つまり，位置に依存しない高い濃度一様性が確認できた．

3) 2D 脳ファントムによる定量精度の評価

Table 2 に，灰白質と白質の局所間カウント比および全灰白質領域と全白質領域のカウント比を示す．灰白質と白質の局所間カウント比は，解像度補正を加えた AC+SC+CDRC によって，比較的構造の大きい領域では，真の比率である 4 に近い値となり，比較的構造の小さい領域でも値が向上し，部分容積効果の改善が見られた．全灰白質領域と全白質領域のカウント比は，AC+SC で 2.7，AC+SC+CDRC で 3.5 となり，CDRC による部分容積効果の改善が確認できた．

4) 3D 脳ファントムによる統計雑音の評価

CDRC を行って複数線線源(水中)を再構成した場合，中央の線線源の解像度は，反復回数 3 回で，CDRC を行わなかった場合の反復回数 5 回の 8.9mm と同程度の 8.3mm となった．

Fig.7 に，CDRC を行わなかった場合と，CDRC を行った場合で，画像再構成の反復回数を変えたときの線線源の解像度と，3D 脳ファントムの CoV との関係を示す．CDRC を行い，CDRC を行わない場合と同程度

Table 2. 2D 脳ファントムにおける白質と灰白質のカウント比

	True	AC+SC	AC+SC+CDRC
GM1/WM1		2.9	4.0
GM1/WM2		1.7	1.9
GM1/WM3		1.7	2.4
GM2/WM1		1.8	4.3
GM2/WM2	4.0	1.1	2.1
GM2/WM3		1.1	2.6
GM3/WM1		2.5	4.1
GM3/WM2		1.4	1.9
GM3/WM3		1.4	2.5
Whole GM/WM	4.0	2.7	3.5

の解像度としたとき，CoV は視床で 17%，脳室で 15%程度まで大きく改善した．この結果から CDRC は，解像度改善効果があるだけでなく，雑音抑制効果もあるといえる．また，CDRC を行い，解像度を 5.4mm 程度とした場合にも，CDRC を行わなかったときより低い CoV となった．

Fig.8 に 3D 脳ファントムの 1 フレームの再構成画像を示す．CDRC を行った場合，反復回数を 3 回としたとき，雑音抑制された画像が得られ，反復回数を 24 回としたとき，高解像度で高コントラストの画像が得られた．

Fig.9 に，CDRC を行わなかった場合と行った場合の CoV 画像を示す．CoV 画像は見やすくするために，3D 脳ファントムの領域外の値は 0 とした．CDRC を行い，CDRC を行わない場合と同程度の解像度となるように反復回数を 3 回としたとき，CoV が大きく低下しており，雑音抑制効果が定量的に確認できた．

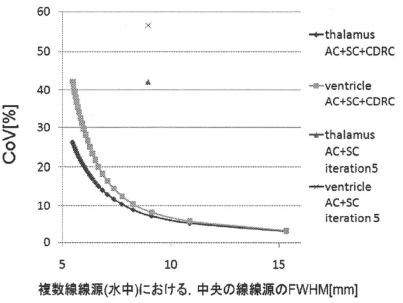

Fig.7 空間解像度と CoV の関係

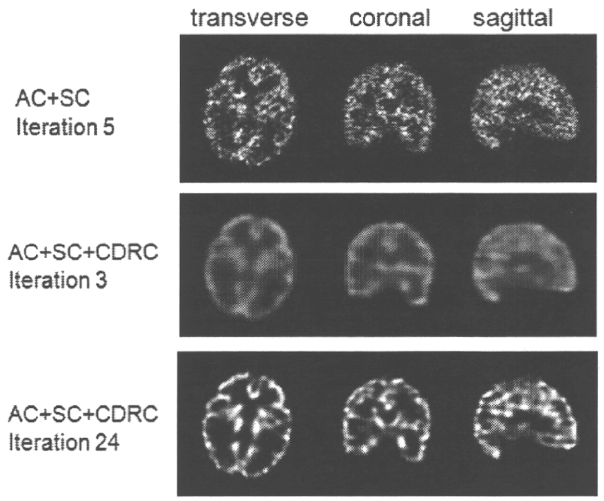

Fig.8 3D 脳ファントム再構成画像

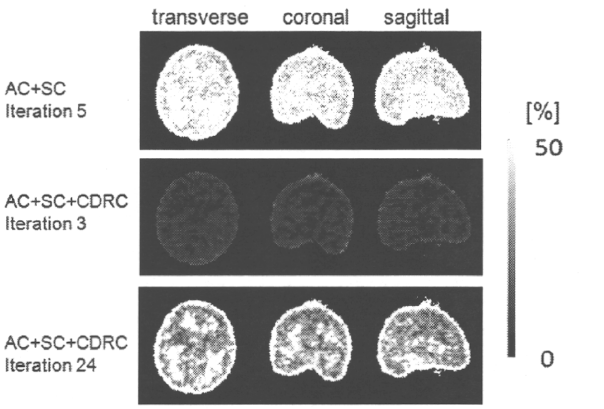

Fig.9 3D 脳ファントム各フレーム間の CoV 画像

5. おわりに

新しい SPECT 画像再構成法の吸収補正と散乱線補正の妥当性が確認できた.コリメータ開口補正により，画像のエッジ部分での Gibbs-like artifact が確認されたものの，解像度は大きく改善した．その結果，部分容積効果の改善することが確認できた．また，コリメータ開口補正は統計雑音抑制効果が有ることも確認できた．これらの結果から，本手法は局所領域の定量評価などに有用であると考えられ，臨床 SPECT 検査の診断精度向上への貢献が期待される．

文　献

[1] A. Sohlberg, H. Watabe and H. Iida, Acceleration of Monte Carlo-based scatter compensation for cardiac SPECT. Phys. Med. Biol. vol.53, no.14, pp.277-285, July 2008.

[2] H. Hudson, R. Larkin, Accelerated image reconstruction using ordered subsets projection data. IEEE Trans. Med. Img. vol.13, Issue.4, pp.100-108, Dec. 1994.

[3] E.V.R. Di Bella, A.B. Barclay, R.L. Einster and R.W. Schafer, A comparison of rotation-based methods for iterative reconstruction algorithms. IEEE Trans. Nucl. Sci. Vol.43, Issue.6, pp.3370-3376, Dec. 1996.

[4] C.E. Metz, F.B.Atkins, R.N. Beck, The geometric transfer function component for scintillation camera collimators with straight parallel holes. Phys. Med. Biol. Vol.25, No.6, pp.1059-1070, Nov. 1980.

[5] G.L. Zeng, G.T. Gullberg, B.M.W Tsui *et al*, Three-dimensional iterative reconstruction algorithms with attenuation and geometric point point response correction. IEEE Trans. Nucl. Sci. Vol.38, Issue.2, pp.693-702, Apr. 1991.

[6] T. Yokoi, H. Shinohara, H. Onishi, Performance evaluation of OSEM reconstruction algorithm incorporating three-dimensional distance-dependant resolution compensation for brain SPECT: A simulation study. Ann. Nucl. Med. Vol.16, No.1, pp.11-18, Feb. 2002.

[7] H. Iida, Y. Narita, H. Kado *et al*, Effects of scatter and attenuation correction on quantitative assessment of regional cerebral blood flow with SPECT. J. Nucl. Med. Vol.39, No.1, pp.191-189, Jan. 1998.

[8] M. Shidahara, H. Watabe, K. Kim *et al*, Impact of attenuation and scatter correction in SPECT for quantification of cerebral blood flow using ^{99m}Tc-Ethyl cystenate dimer. IEEE Trans. Nuc.l Sci. Vol.49, Issue.1, pp.5-11, Feb. 2002.

[9] E. Woodcock, T. Murphy, P. Hemmings *et al*, Techniques used in the GEM code for Monte Carlo neutronics calculations in reactors and other systems with complex geometry. Proc Conf. for applications of computing methods to reactor problems, p.557, 1965.

[10] M. Ljungberg, A. Larsson, L. Johansson: A new collimator simulation in SIMIND based on the Delta-Scattering technique. IEEE Trans. Nucl. Sci. No.52, Issue.5, pp.1370-1375, Oct. 2005.

[11] H.W.A.M. de Jong, E.T.P. Slijpen, F.J. Beekman, Acceleration of Monte Carlo SPECT simulation using convolution-based forced detection. IEEE Trans. Nucl. Sci. Vol.48, Issue.1, pp.58-64, Feb. 2001.

[12] D.J. Kadrmas, E.C. Frey, S.S. Karimi et al, Fast implementation of reconstruction-based scatter compensation in fully 3D SPECT image reconstruction. Phys. Med. Biol. Vol.43, No.4, pp.857-873, Apr. 1998.

[13] E.C. Frey, B.M.W. Tsui, "Collimator-detector response compensation in SPECT," Quantitative analysis in nuclear medicine imaging, H. Zaidi, pp.141-166, Springer Science+Business Media, New York, 2005.

生体医工学
48(5)：459-463, 2010

解説特集：分子イメージング

PET/SPECT 機器・解析技術の進歩

飯田 秀博*・銭谷 勉*・越野 一博*・平野 祥之*

Recent Development in PET/SPECT Equipments and Data Analysis

Hidehiro IIDA,* Tsutomu ZENIYA,* Kazuhiro KOSHINO,* Yoshiyuki HIRANO*

1. はじめに

PETが誕生してから30年以上の技術蓄積の結果，検出器の改良は空間解像度の一桁向上に，多断層化と立体計測技術の普及は感度の二桁上昇に貢献した．SPECTにおいては複数検出器の搭載に加えてコリメータの進歩，さらに画像再構成理論の改善によって精度の確保と画質の改良がなされた．複数モダリティの融合画像処理技術や，新しい画像再構成理論の整備と実用化も進み，また近年はMRIと一体型のPET装置が実用化されるなど技術確認がすすむ．本稿では，新しい要素技術とその効果について概説する．

2. PET

PET装置の空間解像度を決定するのはシンチレーション結晶の大きさであり，小型ブロック検出器の開発が高解像度化に貢献してきた．深さ情報（depth-of-interaction, DOI）を検出する検出器も実用化された．立体計測（3次元，3D）は完全に定着し測定感度は大きく改善し，絶対感度は1%を超えるに至った．臨床PET装置の空間解像度は概ね4 mm程度にまで向上した．画像再構成プログラムはさらに改良が進み，吸収補正や散乱線補正に加えて空間解像度の補正がなされるようになり，空間解像度は2 mm程度になったとされる．高性能な放射線検出シンチレータの実用化がなされ，また同時計測の時間分解能（コインシデンスウインドウ）が短くなった．これは画質劣化の最大の要因であった偶発同時計数の減少に貢献する．一部のメーカーではtime-of-flight計測（同時計測信号の時間差より線源の場所を限局する機構）により，大きな体型の被験者の場合の画質改善に貢献する．

現在の課題は，膨大な情報を高速に処理できる電子回路の開発にあるといえる．PETでは検出器総数の自乗に比例した計測線（line-of-response, LOR）の信号を扱う．典型的には10^8にもなるLOR信号を演算処理・保存するためには相当高速な電子回路技術が必要である．また，3D PET計測における散乱線を補正する普遍的な方法も確立されなければいけない．放射線分布と吸収減弱（μ）分布に物理公式（Klein-Nishinaの式など）を適用する方法が提案されているが，視野外の放射能や散乱線発生の影響についてはまだ系統的に検討されておらず今後の課題である．当該研究グループ平野らは限りなく忠実に放射線の輸送を再現するプログラムコードの開発に成功し，これにより散乱線は被写体内だけでなく床壁やPET装置自身によっても発生することが明らかになった．正確な補正を実現するプログラムの開発やシールド機構の設計などにおいて，系統的な検証が可能になったところである．

3. SPECT

SPECT技術の最近の重要な進展は，定量化と標準化に対する道筋が明らかになったことであろう．SPECT画像の定量精度の確保は従来から困難とされてきたが，吸収と散乱線を正確に補正する実用的なプログラムの整備によって正確な画像が得られるようになった．本来ふたつの誤差は被写体内部で発生するため装置には依存しない．PETでは散乱線分布は装置の幾何学に依存することと対象的に，SPECTの重要な特長である．すなわち吸収と散乱線を補正するソフトウエアが整備されれば，その時点でメーカーや機種を超えた再現性が得られることを意味する．これは臨床機関を超えてデータが共有できる点においても，また既存の装置がそのまま利用できる点においても，

* 国立循環器病研究センター研究所先進医工学部門画像診断医学部
Department of Biomedical Imaging, National Cerebral and Cardiovascular Center Research Institute